PCCP

Accepted Manuscript

ROYAL SOCIETY OF CHEMISTRY

www.rsc.org/pccp

Thermally-induced single-crystal-to-single-crystal transformations from 2D two-fold interpenetrating square lattice layer to 3D four-fold interpenetrating diamond framework and its application in dye-sensitized solar cells

Song Gao, Rui Qing Fan,* Xin Ming Wang, Li Guo Wei, Yang Song, Xi Du, Kai Xing, Ping Wang, Yu Lin Yang*

MIIT Key Laboratory of Critical Materials Technology for New Energy Conversion and Storage, School of Chemistry and Chemical Engineering, Harbin Institute of Technology, Harbin 150001, P. R. China

To whom the proofs and correspondence should be sent.

Professor Rui-Qing Fan
School of Chemistry and Chemical Engineering
Harbin Institute of Technology Harbin 150001, P. R. China
Fax: +86-451-86413710
E-mail: fanruiqing@hit.edu.cn and ylyang@hit.edu.cn

Abstract In this work, a rare 2D→3D single-crystal-to-single-crystal transformation (SCSC) is observed in metal-organic coordination complexes, which is triggered by thermal treatment. The 2D two-fold interpenetrating square lattice layer $[Cd(IBA)_2]_n$ (**1**) is irreversibly converted into a 3D four-fold interpenetrating diamond framework $\{[Cd(IBA)_2(H_2O)]\cdot 2.5H_2O\}_n$ (**2**) (HIBA = 4-(1H-imidazol-1-yl)benzoic acid). Consideration two complexes with different interpenetrating structures and dimensionality, their influence on photovoltaic properties are studied. Encouraged by the UV-visible absorption and HOMO–LUMO energy states matched for sensitizing TiO_2, the two complexes are employed in combination with N719 in dye-sensitized solar cells (DSSCs) to compensate absorption in the region of ultraviolet and blue-violet, offset competitive visible light absorption of I_3^- and reducing charge recombination of injected electron. After co-sensitized with **1** and **2**, the device co-sensitized by **1**/N719 and **2**/N719 yield an overall efficiency of 7.82% and 8.39%, which are 19.94% and 28.68% higher than that of the device sensitized only by N719 (6.52%). Consequently, high dimensional interpenetrating complexes could serve as excellent co-sensitizers and application in DSSCs.

Introduction

Currently single-crystal-to-single-crystal (SCSC) transformations have attracted the greatest attention in solid-state chemistry and crystal engineering.[1–4] In the process of crystal growth and post-synthetic treatment, due to the tension and shear forces produced by component changes, the brittle single crystal tends to increase mosaicity and even crack into smaller specimen under various chemical and physical stimuli. Such phenomena may become more serious for many flexible complexes exhibiting very significant structural changes. Through the SCSC transformation, new complexes can be gained in a high yield, which cannot be obtained under conventional conditions. Therefore, SCSC transformation is of particular significance and interest.[5–8] Hitherto, a variety of SCSC transformations, such as 0D → 1D/2D, 1D → 2D/3D, and 2D → 3D have been documented.[9–12] These types of structural transformations are associated with the cleavage and regeneration of new coordination bonds and the corresponding change in dimensionality is reflected by small changes in porosity, and optical and thermal stability.[13] In particular, structural transformations involving 2D and 3D frameworks are the more important because most of the complexes with potential properties–such as sensor, catalysis, magnetism, and gas storage, separation–are generally 3D frameworks.[14,15] Meanwhile, the SCSC transformations between interpenetrating structures are still quite rare, since it is difficult to retain their crystallinity after breaking and forming coordination bonds in the solid phase due to interpenetrating structure stability.[16] Therefore, the design and fabrication of the SCSC transformation between 2D → 3D interpenetrating

structures is still a big challenge.

Based on this idea, we considered Cd(II) to be a good candidate for construction of complexes due to its more fascinating mode of coordination (coordination number 4-8), lower-cost and adequate electron transport, of which the complexes have a variety of structures and favorable properties.[17-21] The enormous variabilities of available ligand–metal combinations open the possibility of creating SCSC transformations "by design". 4-(1H-imidazol-1-yl)benzoic acid (HIBA), with the torsional space between the benzene ring and the imidazole ring, is a versatile ligand with the ability to form interpenetrating structure due to the position of its functional groups.[22,23] Inspired by this, the reaction strategy of a thermally induced SCSC transformation, the 2D two-fold interpenetrating square lattice layer $[Cd(IBA)_2]_n$ (**1**) is successfully converted to a 3D four-fold interpenetrating diamond framework $\{[Cd(IBA)_2(H_2O)]\cdot 2.5H_2O\}_n$ (**2**) *via* addition of the coordinated water molecule and rearrangement of coordination bonds. Within the reaction of the HIBA with Cd(II) ion under thermal treatment condition, the water existed in solvent may easier to coordinate with the metal center.

As the rapid development of energy conversion devices, the complexes are being applied in the dye sensitized solar cells (DSSCs) gradually. In the photoelectric transformation, co-sensitization by means of multiple sensitizers including complexes would appear to be more effective to improve the absorption ability of solar cell.[24] It is found that complexes with large surface area and interconnected molecules will help to adsorb sufficient dye and provide a pathway for the transport of electrons, and further improve the photovoltaic properties of DSSCs when they are used as co-sensitizers. Therefore, the synthesis of co-sensitizers with high dimensional and pore structures is very important. The structural transformation of one of these complexes is accompanied by SCSC manner which helps to get high dimensional structure and framework porosity.[25,26] For example, Yang and coworkers described an exceedingly rare example of solid-state SCSC transformation from a 2D layer to a known 3D framework, which brings the free volume up to 33.7%.[27] The colleagues of Lin and Wen obtained SCSC transformation of the 2D coordination network to the 3D metal–organic framework *via* dimerization of the metal-connecting points, leading to significant enhancement in framework porosity.[28] To the best of our knowledge, high dimensional interpenetrating complexes as co-sensitizers are never investigated. A high dimensional interpenetrating structure might exhibit high thermal stability and porosity. It is beneficial to adsorb dye molecules to enhance efficient light harvesting. The excellent properties indicate the great potential of the high dimensional interpenetrating complexes being utilized as co-sensitizers in DSSCs fields. In addition, considering ruthenium complex N719 as a typical

representative of organic dye used in DSSCs with low utilization in the region of short wavelength, the complexes as co-sensitizers could not only compensate the absorption spectra but also overcome the competitive light absorption by I^-/I_3^-, avoid dye aggregation and reduce charge recombination, which will lead to enhanced DSSCs performance.[29] On the basis of the above considerations, this work initially attempts to use high dimensional interpenetrating complexes as co-sensitizers for detailed research. Complexes **1** and **2** are employed as co-sensitizers with N719 dye based solar cell, and the co-sensitized devices exhibit enhancements of photovoltaic performance. The power conversion efficiency of N719 sensitized DSSCs is enhanced by 19.94% and 28.68% after co-sensitized with **1** and **2** than that for DSSCs using single N719. As a consequence, the reasonable design and synthesis of high dimensional interpenetrating complexes with a combination of different optical and electrochemical properties may provide interesting insight into the development of high-performance DSSCs devices.

Experimental section

Materials and Measurements

All materials and reagents were commercially available and used without further purification. IR spectra were obtained from KBr pellets using a Nicolet Avatar-360 infrared spectrometer. Elemental analyses were performed on a Perkin-Elmer 2400 element analyzer. Powder X-ray diffraction (PXRD) patterns were recorded in the 2θ range of 5–50° using Cu Kα radiation by Shimadzu XRD-6000 X-ray Diffractometer. The thermal analyses were performed on a ZRY-2P thermogravimetric analysis under a flow of air from room temperature to 700 °C. Variable-temperature X-ray powder diffraction (VT-XRPD) patterns were obtained using a PANalytical X-ray diffractometer, equipped with monochromated Cu Kα radiation 40 mA, 40 kV. UV-visible absorption spectra were recorded on SPECORD S600 spectrophotometer (Jena, Germany) for samples in ethanol solution and UV-2250 spectrophotometer (Shimadzu, Japan) for sensitized TiO_2 films, respectively. The solid-state photoluminescence analyses were carried out on an Edinburgh FLS920 fluorescence spectrometer. The cyclic voltammetry (CV) were measured with a electrochemical workstation (CHI660D, Chenhua, Shanghai) using a three-electrode cell with a Pt working electrode, a Pt wire auxiliary electrode, and a saturated calomel reference electrode in saturated KCl solution. The supporting electrolyte was 0.1 M tetrabutylammonium hexafluorophosphate ($TBAPF_6$, Fluka, electrochemical grade) in ethanol as the solvent. Photocurrent-photovoltage (*J-V*) curves were recorded by Keithley model 2400 digital source meter using a mask with an aperture area of 0.16 cm^{-2}. The incident photon-to-current conversion efficiency (IPCE) was measured on an EQE/IPCE spectral response system (Newport). Electrochemical impedance spectroscopy (EIS) was recorded by

CHI660D Electrochemical Analyzer (Chenhua, China).

Assembly of DSSCs

The FTO conducting glass (Fluorine-doped SnO_2, sheet resistance 15 Ω per square, transmission 90% in the visible) was purchased from NSG, Japan, and cleaned by a standard procedure. N719 [*cis*-bis(isothiocyanato)bis (2,2-bipyridyl-4,4-dicarboxylato)-ruthenium(II)bis-tetrabutylammonium] was purchased from Solaronix Company, Switzerland. Dye-sensitized solar cells were fabricated using the following procedure. Before screen-printing method, FTO substrate was first treated by 20 mM $TiCl_4$ aqueous solution in order to reduce the recombination between FTO and electrolyte. The TiO_2 paste was cast onto the FTO substrate by the screen-printing method, and the FTO substrate was treated by 20 mM $TiCl_4$ aqueous solution again to optimize the TiO_2 thin film, followed by drying at 100 ºC for 5 min and this process was repeated for six times, then followed by sintering at 500 ºC for 15 min in air to obtain a transparent TiO_2 photoelectrode with the thickness of ca. 10 μm. The co-adsorbent electrodes were prepared by immersing the obtained mesoporous TiO_2 photoelectrode into 0.3 mM **1** or **2** solution in absolute ethanol for 2 h and washed with ethanol and dried with blower, then further immersing the electrodes in 0.3 mM N719 solution in absolute ethanol for 12 h, and then washed with ethanol and dried with blower again. The single N719 sensitized electrodes were prepared by only immersing TiO_2 photoelectrode into 0.3 mM N719 solution in absolute ethanol for 14 h. The electrolyte used in this work was 0.5 M LiI + 0.05 M I_2 + 0.1 M *tert*-butyl pyridine in a 1:1 (volume ratio) of acetonitrile-propylene carbonate. The platinum counter electrode was prepared by depositing H_2PtCl_6 paste onto the FTO glass substrates and then sintered at 450 ºC for 30 min. The cells were assembled by sandwiching the electrolyte between the dye sensitized photoanode and the counter electrode and assembly was held together using mini-binder clips.

Synthesis of $[Cd(IBA)_2]_n$ (1) and $\{[Cd(IBA)_2(H_2O)]\cdot 2.5H_2O\}_n$ (2)

A mixture of $Cd(NO_3)_2\cdot 4H_2O$ (92.4 mg, 0.3 mmol), HIBA (18.8 mg, 0.1 mmol) were dissolved in 8 mL H_2O, and stirred for 30 min, then heated in a sealed vial at 80 °C for 6 days. After slow cooling to room temperature, flavescens block crystals of **1** were obtained with a yield of 77% (based on HIBA). Anal. Calcd for $C_{20}H_{14}N_4O_4Cd$ (*Mr*: 486.75): C, 49.35; H, 2.90; N, 11.51%. Found: C, 49.38; H, 2.91; N, 11.50%. IR (KBr pellet, cm^{-1}, Fig. S1) for **1**: 3436 (br, s), 1698(s), 1609 (vs), 1526(s), 1484(m), 1427(w), 1306(s), 1243(m), 1181(m), 1114(m), 1055(s), 957(s), 847(m), 774(vs), 691(m), 643(s), 524(vs). Freshly prepared block-type single crystals **1** were transferred into a 15 mL Teflon-lined stainless steel autoclave and heated to 200 ºC for 24 h. Flavescens sheet crystals **2** were obtained with a yield of 69% (based on HIBA). Anal. Calcd for $C_{20}H_{21}N_4O_{7.5}Cd$ (*Mr*: 549.82): C, 43.69; H,

3.85; N, 10.19%. Found: C, 43.46; H, 3.82; N, 10.17%. IR (KBr pellet, cm^{-1}, Fig. S1) for **2**: 3420 (br, s), 1672(s), 1604 (s), 1552(s), 1520(s), 1401(vs), 1302(s), 1244(w), 1181(w), 1124(m), 1056(s), 967(m), 852(s), 774(s), 696(w), 649(m), 508(m).

X-ray Crystallography

The X–ray diffraction data taken at room temperature for complexes **1** and **2** were collected on a Rigaku R–AXIS RAPID IP diffractometer equipped with graphite–monochromated Mo Kα radiation (λ = 0.71073 Å). The structures of **1** and **2** were solved by direct methods and refined on F^2 by the full–matrix least squares using the SHELXTL–97 crystallographic software.[30,31] Anisotropic thermal parameters are refined to all of the non–hydrogen atoms. The hydrogen atoms were held in calculated positions on carbon atoms and nitrogen atoms and that were directly included in the molecular formula on water molecules. The CCDC 1041925, 1041924 contain the crystallographic data **1** and **2** of this paper. These data can be obtained free of charge at www.ccdc.cam.ac.uk/ deposit. Crystal structure data and details of the data collection and the structure refinement are listed as Table 1, selected bond lengths and bond angles of **1** and **2** are listed as Table S1.

Table 1 Crystal data and structure refinement parameters of complexes **1** and **2**

Identification code	**1**	**2**
Empirical formula	$C_{20}H_{14}N_4O_4Cd$	$C_{20}H_{21}N_4O_{7.5}Cd$
Formula mass	486.75	549.82
Crystal system	Orthorhombic	Orthorhombic
Space group	*P*nna	*P*bcn
a (Å)	13.846(3)	15.882(1)
b (Å)	16.556(3)	17.505(2)
c (Å)	8.239(2)	17.870(1)
α (°)	90.00	90.00
β (°)	90.00	90.00
γ (°)	90.00	90.00
V ($Å^3$)	1888.7(6)	4968.2(7)
Z	4	8
D_c/(g · cm^{-3})	1.712	1.470
μ (Mo Kα)/mm^{-1}	1.192	0.925
F(000)	968	2216
θ range (°)	3.13 – 27.48	3.04 – 25.36
Limiting indices	$-17 \le h \le 17$ $-21 \le k \le 21$ $-10 \le l \le 10$	$-17 \le h \le 19$ $-19 \le k \le 20$ $-17 \le l \le 21$
Data/Restraints/Parameters	2156 / 0 / 132	4502 / 0 / 298
GOF on F^2	1.060	1.043
Final *R* indices [$I > 2\sigma(I)$]		
R_1[a]	0.0318	0.0875
wR_2[b]	0.0816	0.1531
R indices (alldata)		
R_1	0.0419	0.1087
wR_2	0.0865	0.1917
CCDC	1041925	1041924

[a] $R_1 = \sum||F_o| - |F_c|| / \sum|F_o|$; [b] $wR_2 = [\sum[w (F_o^2 - F_c^2)^2] / \sum[w (F_o^2)^2]]^{1/2}$.

Results and discussion

Structure description: $[Cd(IBA)_2]_n$ (1)

Complex **1** contains one Cd^{2+} cation, two IBA^- anions in the asymmetric unit (Fig. 1a). X-ray analysis reveals that the central Cd^{2+} cation is six-coordinated and forms distorted triangular prism coordination geometry, completed by four oxygen atoms from carboxylate and two nitrogen atoms from imidazole groups (Fig. 1b). In **1**, the carboxylate group is completely deprotonated and adopts a bidentate-chelate fashion. The imidazole ring and phenyl rings of IBA^- in a nonplanar fashion, form to left-handed helices (Fig. 1c). The resulting left-handed helices with a pitch of 16.478 Å are alternately arranged in an equal ratio, extending into a 2D layer structure (Fig. 1d).

Fig. 1 (a) Asymmetric unit of **1** (hydrogen atoms are omitted for clarity). Symmetry codes: O1A 1.5-*x*, -*y*, -1+*z*; O1B 1.5-*x*, -0.5+*y*, 1.5-*z*; O2A 1.5-*x*, -*y*, -1+*z*; O2B 1.5-*x*, -0.5+*y*, 1.5-*z*; N1A *x*, -0.5-*y*, 0.5-*z*; N1B 1.5-*x*, -*y*, -1+*z*; N2A *x*, -0.5-*y*, 0.5-*z*. (b) Polyhedral representation of the coordination sphere of the Cd^{2+} centre in **1**. (c) The space-filling mode of the left-handed helix in **1**. (d) The illustration of single 2D layer in **1**.

The 2D layer contains two separated sub-layers with the Cd^{2+} cation in a common plane. Two of sub-layers are further parallel to each other. Thus, a two-fold parallel interpenetrating

crystalline lattice is afforded (Fig. 2a). Every separated sub-layer is constructed by infinite square grids. Thus, **1** exhibits a square grid with square dimensions of 16.478(3) × 16.556(3) Å. If the Cd^{2+} cation is considered as a 4-connected node and the IBA^- anions as the linkers, then **1** is simplified to a 4-connected 2D **sql** topological network with the Schläfli symbol of $(4^4.6^2)$. The layers are further stabilized by π–π stacking interaction between adjacent imidazole rings with distances of 3.495 Å (Fig. 2b).

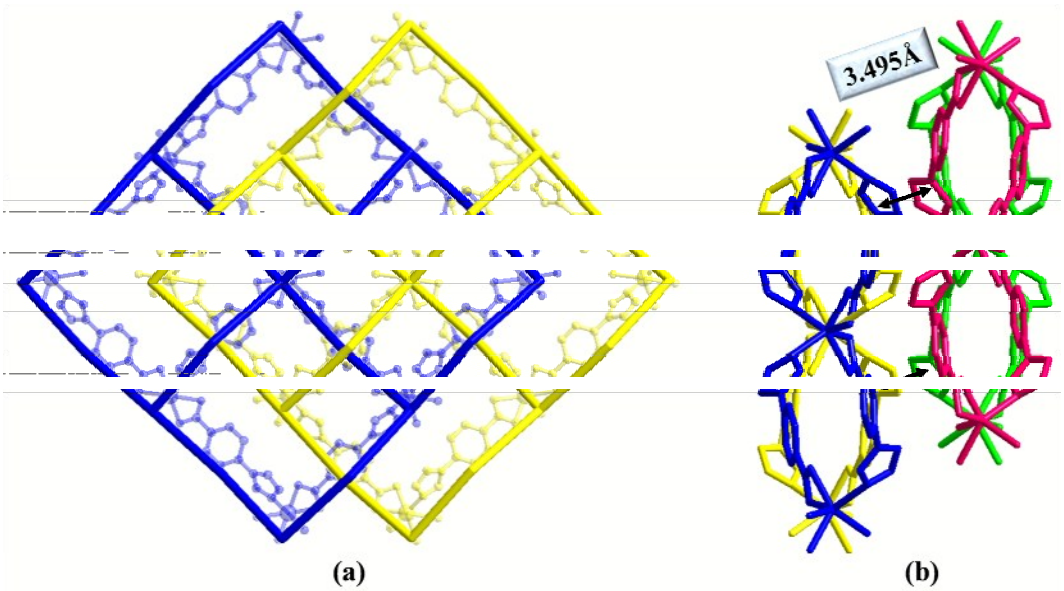

Fig. 2 (a) The ball-and-stick and the topological representation of a two-fold parallel interpenetrating layer of **1**. (b) The π-π interactions between the two face-to-face imidazole rings of IBA^- anion.

Structure description: $\{[Cd(IBA)_2(H_2O)]\cdot 2.5H_2O\}_n$ (2)

The asymmetric unit of complex **2** contains one Cd^{2+} cation, two IBA^- anions, one coordinated water molecule, and two and half free water molecules (Fig. 3a). The Cd1 has a pentagonal bipyramid environment, in which contains O1, O2, O3, O4, O5, N1 and N3 from two IBA^- anions and one coordinated water molecule (Fig. 3b). In **2**, each IBA^- anion links two adjacent Cd^{2+} cations, and four IBA^- anions coordinated to one Cd^{2+} cation have a pseudotetrahedral extension. Thus, a 3D diamond-like network is formed, containing large adamantanoid cages (Fig. 3c). A single adamantanoid cage exhibits maximum dimension of 35.011(2) Å × 21.815(1) Å (corresponding to the longest intracage Cd···Cd distances). Given that the chelating carboxylates are treated as one connecting point, each Cd^{2+} cation is connected to four adjacent Cd^{2+} cations through the four linear IBA^- linkers to result in a 3D **dia** topology with the point symbol 6^6 and the long symbol $6_2\cdot6_2\cdot6_2\cdot6_2\cdot6_2\cdot6_2$ (Fig. 3d).

In order to minimize the big hollow cavities in **2** and stabilize the overall network, the huge chamber facilitates other three independent equivalent networks to interpenetrate, generating a four-fold interpenetrated 3D architecture (Fig. S2). Topologically, the structure of

2 consists of **dia** framework, and four independent **dia** nets are interpenetrated within the whole structure (Fig. 4). The total void value of the channel without free water molecules is estimated to be 1278.6 Å^3 by *PLATON*[32,33] software, approximately 25.7% of the total crystal volume of 4968.2 Å^3.

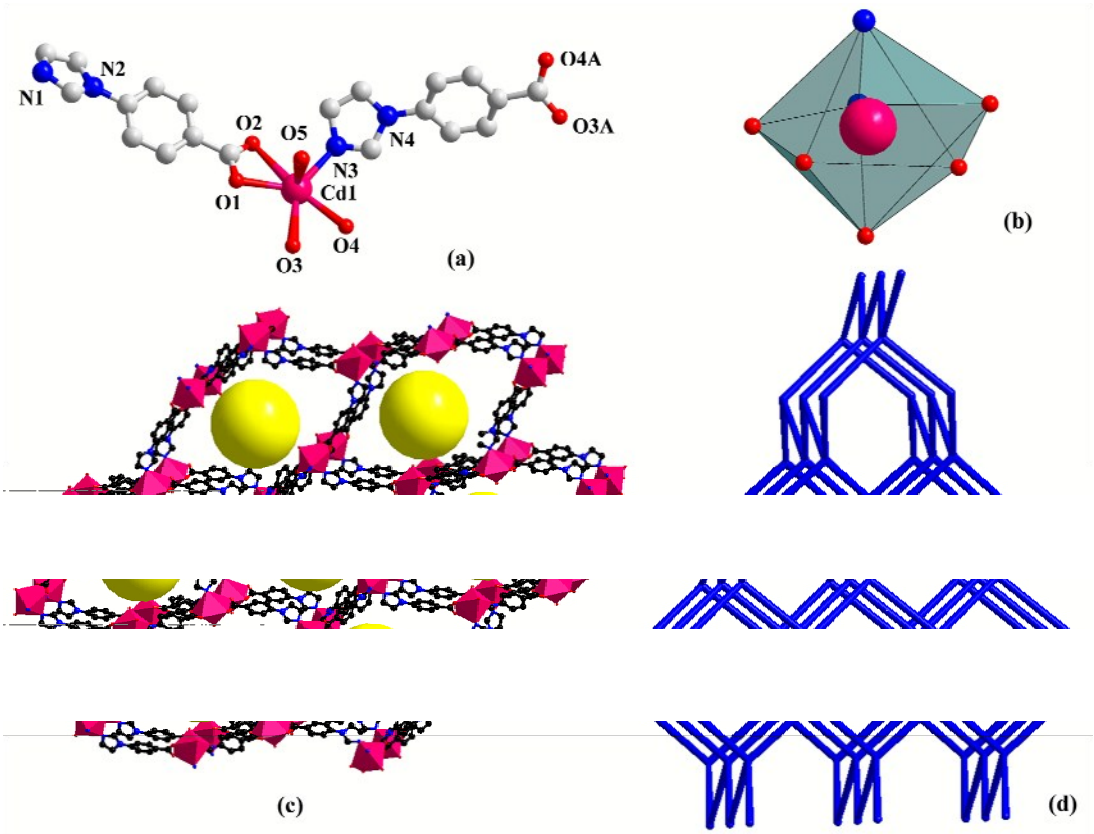

Fig. 3 (a) Asymmetric unit of **2** (hydrogen atoms are omitted for clarity). Symmetry codes: O3A 0.5-*x*, 0.5-*y*, 0.5+*z*; O4A 0.5-*x*, 0.5-*y*, 0.5+*z*. (b) Polyhedral representation of the coordination sphere of the Cd^{2+} centre in **2**. (c) View of the 3D framework structure of **2**. (d) Schematic representation of 6^6-**dia** topology for **2**.

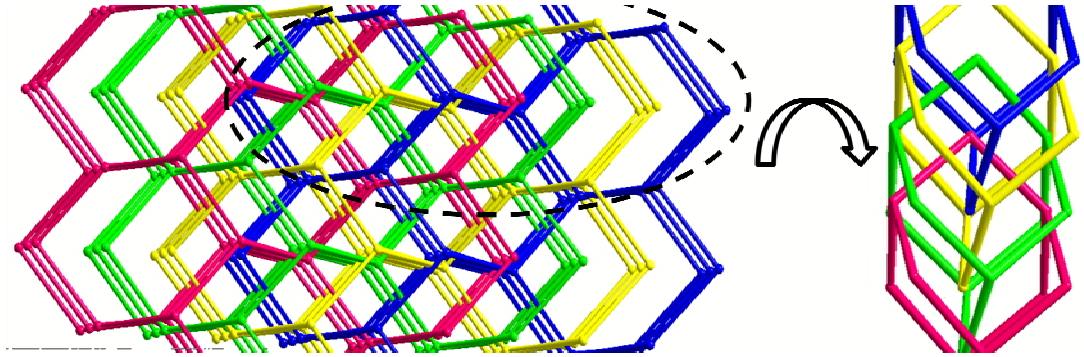

Fig. 4 Schematic representation of the four-fold interpenetrated 3D 6^6-**dia** topology of **2**.

Comparison of synthetic conditions and structures

The single-crystal-to-single-crystal transformations can be achieved by thermal treatment, the 2D complex $[Cd(IBA)_2]_n$ (**1**) is successfully converted to 3D complex $\{[Cd(IBA)_2(H_2O)]\cdot 2.5H_2O\}_n$ (**2**) *via* breakage/formation of chemical bonds. This SCSC phase transition could provide us a good model to study the correlation between the changes in the crystal interior and its morphology.[34,35] **1** was prepared using $Cd(NO_3)_2\cdot 4H_2O$ and HIBA ligand at 80 °C under hydrothermal synthetic conditions. As expected, upon heating to 200 °C under Teflon-lined stainless steel autoclave, **1** undergoes a SCSC transformation to yield the **2**. The result of single-crystal X-ray diffraction analysis revealed that **1** and **2** crystallizes in the orthorhombic space group. The most significant molecular transformation is that the six-coordinated triangular prism coordination geometry of Cd(II) cation in **1** change to the seven-coordinated pentagonal bipyramid coordination geometry of Cd(II) cation in **2**, where one of the oxygen atoms takes on an additional Cd–O5 (coordinated water molecule) interaction to become (2.463(3) Å, 2.279(2) Å, 2.463(3) Å and 2.279(2) Å for **1** vs. Cd–O = 2.394(1) Å, 2.485(1) Å, 2.320(1) Å and 2.644(1) Å for **2**). This leads to the distances change of the intermolecular oxygen atom-to-oxygen atom (2.187(1) Å, 3.649(2) Å, 2.187(1) Å and 3.649(2) Å for **1** vs. 2.218(1) Å, 3.325(2) Å, 2.208(3) Å and 4.987(1) Å for **2**); nitrogen atom-to-nitrogen atom (3.214(2) Å for **1** vs. 3.476(2) Å for **2**) (Fig. 5). Consequently, the existence of coordinated water molecule led us to explore possible SCSC transformation. The above structure analysis implies that the transformation between **1** and **2** involves changes of lattice parameters, bond reformation, and coordination geometry of the Cd(II) site. Note that in the literature the instance of SCSC from 2D layer to 3D framework interpenetrating structures has little been established.

Powder X-ray diffraction (PXRD) and thermogravimetric analysis (TGA) studies

PXRD has been used to check the phase purity of the bulky samples in the solid state. As shown in Fig. S3, the experimental PXRD patterns of complexes **1** and **2** are in good agreement with the simulated patterns, which indicate the good phase purity of complexes **1** and **2**. The differences in intensity may be due to the preferred orientation of the crystalline powder samples.[36,37] To confirm the simultaneous structural transformation with the breaking/forming of the coordination bonds process, complex **1** is heated to 110 °C, 140 °C, 170 °C, 200 °C and 220 °C then analyzed with PXRD (Fig. 6). Upon heating, the pattern suddenly changed at 200 °C. The pattern of heating was consistent with the simulated pattern generated by the crystallographic data of **2**. This **2** was maintained upon cooling to 80 °C, this process was unsuccessful; therefore, this SCSC conversion is irreversible.[38] Thermogravimetric experiments were conducted to study the thermal stability of complexes **1** and **2** (Fig. S4).[39–41] The TGA curve shows that **1** has one weight–loss stage. The weight–loss

of 76.26% in the temperature range of 271~319 °C is attributed to the loss of two HIBA ligands. The value is close to the calculated value of 77.32%. In the TGA curve of **2**, there are two continuous weight–loss steps. The weight loss of 9.52% in the temperature range of 342~378 °C corresponds to the one coordination water molecule and two and half free water molecules which is in accordance with the calculated value of 11.47%. The second weight–loss of 68.18% at 411~462 °C is considered as the two HIBA ligands (calcd: 68.45%).

Fig. 5 The detailed structure change of **1** and **2** structures and the coordination geometry of Cd(II) ions involved in this SCSC transformation.

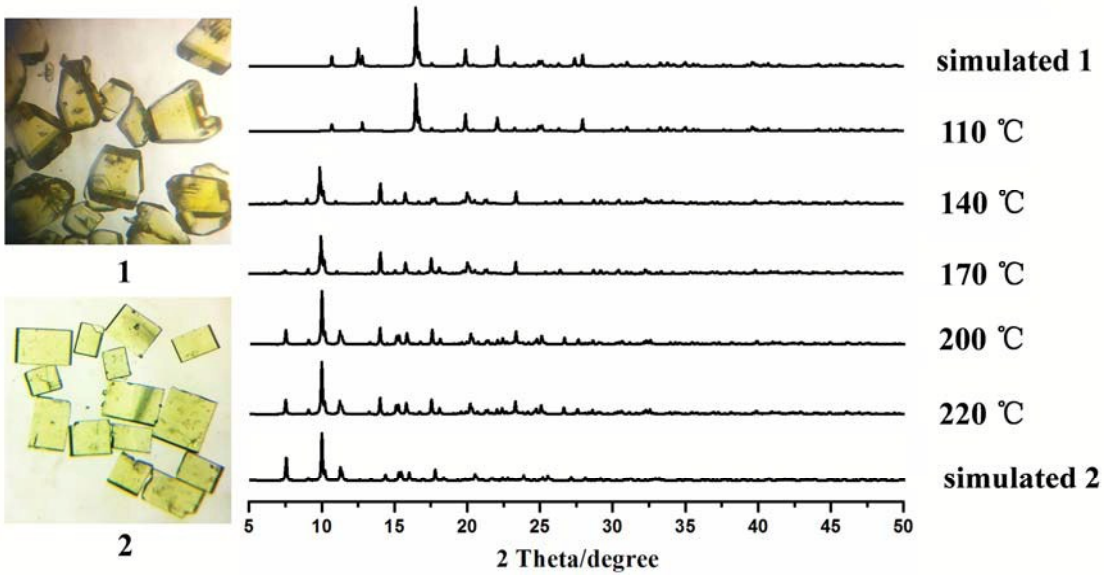

Fig. 6 Photographs of the crystal transformation from **1** to **2**, and the powder X-ray diffraction patterns in the process of crystal transformation.

Optical properties of complexes 1 and 2

Fig. 7a shows the UV-visible absorption spectra of the two complexes and N719 in ethanol solution and the corresponding data are listed in Table 2. Complexes **1** and **2** display strong absorption bands at 335 nm and 352 nm with weak absorption peaks at 380 nm and 386 nm, respectively. Compared with the absorption spectrum of N719, the absorption spectra of **1** and **2** could compensate for that of N719 in the low wavelength region of ultraviolet and blue-violet. More importantly, the molar extinction coefficients in the blue-violet region are 41333 M^{-1} cm^{-1} for **1** and 46643 M^{-1} cm^{-1} for **2**, which are much higher than that of the ruthenium complex N719.[42,43] Such higher molar extinction coefficients indicate **1** and **2** possess higher light harvesting ability in this wavelength region compared with N719 and I_3^- (25,000M^{-1} cm^{-1}).[44] To confirm the compensated and suppressed function of **1** and **2**, the absorption spectra of **1**/N719 and **2**/N719 sensitized TiO_2 films are recorded and shown in Fig. 7b. The TiO_2 films co-sensitized by N719 and the prepared complexes led to surprising results in their absorption spectra in the visible region.[45,46] The two clear absorption bands of N719 in ethanol solution at 383 and 525 nm are broadened at both sides when it attaches to the TiO_2 film, indicating the formation of Herring-bone aggregates by N719 on the TiO_2 nanocrystal surface. When any one of the prepared complexes is incorporated into the N719 sensitized TiO_2 film, the intensities of the two characteristic absorption bands increase a lot. Besides, the two absorption bands at 554 and 367 nm attributed to N719 move to 546 and 372 nm for **1** (552 and 383 nm for **2**), respectively, suggesting that the aggregation degree of N719 on the TiO_2 film has decreased. The alleviation of aggregates adjusts the arrangement of N719 molecules toward a more uniform orientation and formed a compact layer with complexes.[47] Apparently, the increment of the absorption intensity of the TiO_2 films after co-sensitization will contribute to their spectral responses as well as the power conversion efficiency of the DSSCs.

The emission spectra of **1** and **2** are illustrated in Fig. 8. All of them exhibit strong fluorescence in the region of wavelengths 350–750 nm, and it is worth noting that all of the emission spectra of **1** and **2** overlap with the excitation spectra of N719 inordinately. This indicates that N719 could synchronously accept the energy from the incident light and the excited complexes, which will broaden the spectral response of N719 in the region of 350–750 nm.

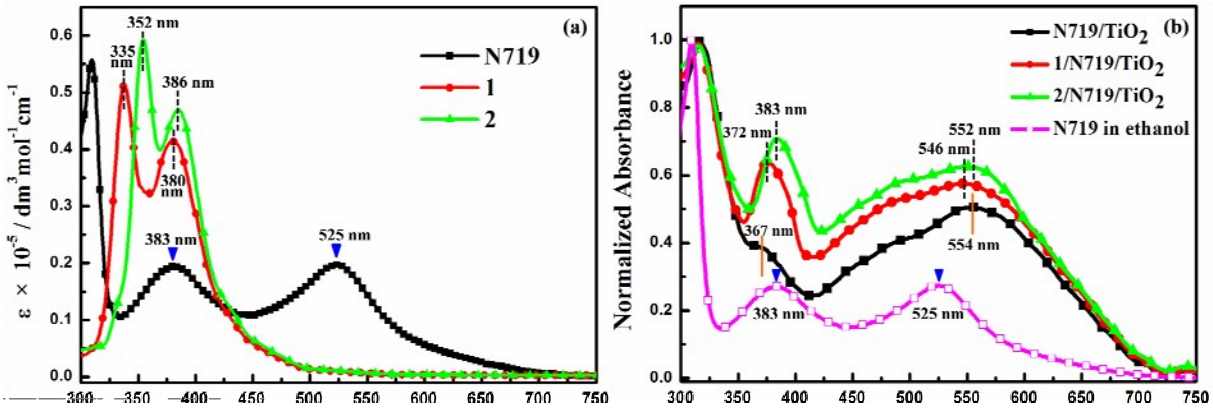

Fig. 7 UV-visible absorption spectra of **1**, **2** and N719 (a) in ethanol, (b) on TiO_2 films.

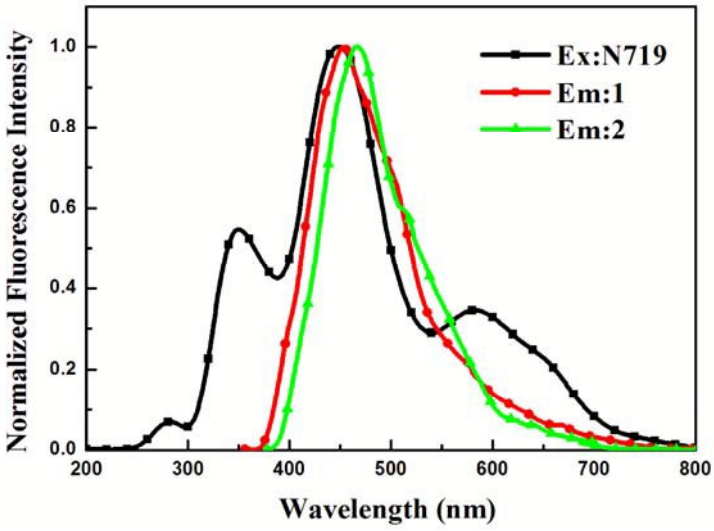

Fig. 8 The emission spectra of **1** and **2** in ethanol solution.

Electrochemical properties of complexes 1 and 2

Energy-level matching is greatly crucial for co-sensitizer materials used in DSSCs. The highest occupied molecular orbital (HOMO), lowest unoccupied molecular orbital (LUMO) energy levels and the excitation transition energy (E_{0-0}) can be calculated conveniently by equations as follows:[48]

$$\text{HOMO (eV)} = -e(E^{ox}_{onset}\text{V} + 4.4\text{V}); \quad \text{LUMO (eV)} = E_{HOMO} + E_{0\text{-}0}$$

As estimated from the intersection of the normalized absorption and emission spectra, the E_{0-0} value is 3.05 eV for **1** and 2.99 for **2**. As shown in Fig. S5, from the onset of the ground state oxidation peak in the cyclic voltammetry (CV), the HOMO value of **1** and **2** are calculated as −5.31 eV and −5.22 eV, respectively. Thus, the LUMO level of **1** and **2** are estimated to be −2.26 eV and −2.23 eV, respectively. For efficient electron injection and regeneration of the photo-oxidized dye, the LUMO level of a sensitizer should lie above the energy level of the conduction band (CB) of the TiO_2 semiconductor (−4.40 eV *vs.* vacuum) and its HOMO

energy level should lie below the energy level of the I^-/I_3^- redox couple in the presence of 4-*tert*-butyl pyridine (−4.85 eV *vs.* vacuum).[49,50] The LUMO levels of the **1** and **2** are higher than that of N719 and the conduction band of TiO_2, which conduce to an enhanced injection driving force of electrons compared with alone N719.[51] Therefore, the positive synergistic effect of these complexes and N719 improves the electrons injection efficiency from the LUMO of dye to the conduction band of TiO_2. The experimental data are summarized in Table 2 and the HOMO and LUMO energy levels of **1** and **2** are shown in Scheme 1. Thus, the suitability of **1** and **2** as co-sensitizers in TiO_2 based DSSCs can be considered.

Table 2 Experimental data for spectral and electrochemical properties of complexes **1** and **2**

Complexes	λ_{abs}(nm)[a]	$\varepsilon(M^{-1}cm^{-1})$[a]	λ_{em}(nm)[a,b]	E_{0-0}(eV)[c]	E_{ox}/V_{vs} SCE[d]	E_{HOMO}(eV)	E_{LUMO}(eV)
1	380	41333	453	3.05	0.91	–5.31	–2.26
2	386	46643	467	2.99	0.82	–5.22	–2.23

[a] Absorption and emission spectra were recorded in ethanol solution (10^{-5} M) at room temperature.
[b] Complexes were excited at their absorption maximum value.
[c] Optical band gap calculated from intersection between the absorption and emission spectra.
[d] The first oxidation potentials of complexes were obtained by CV measurement.

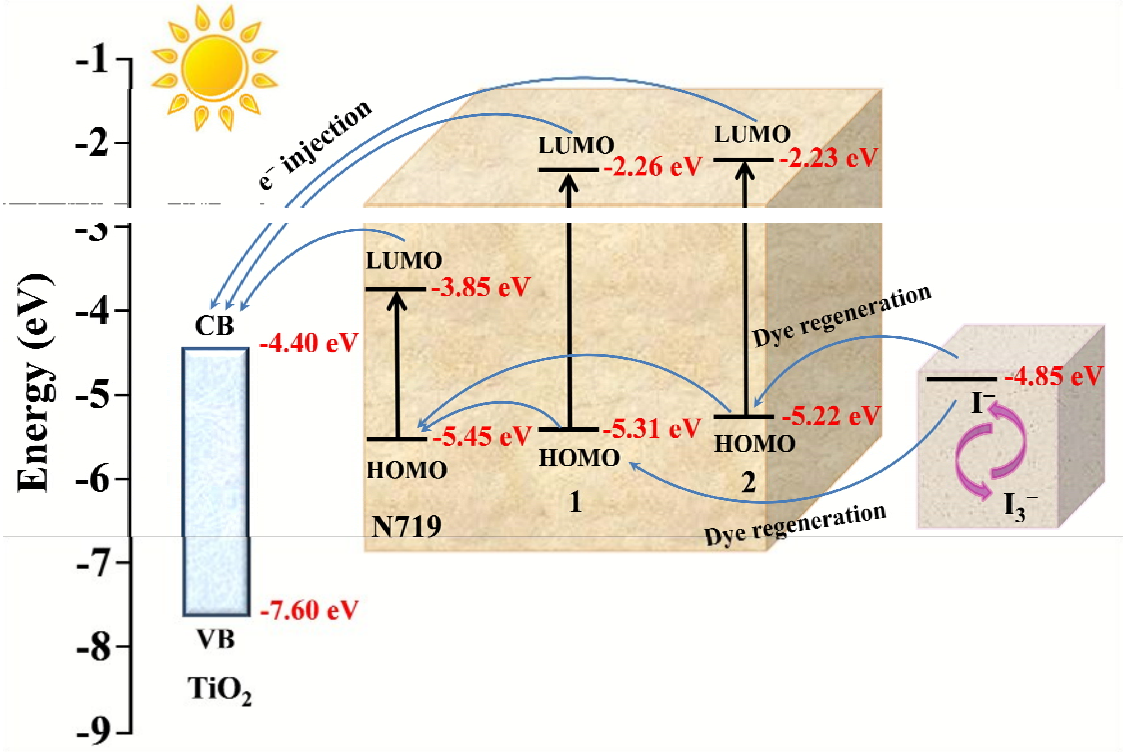

Scheme 1. Schematic energy diagram of HOMO and LUMO for dyes compared to the energy levels calculated for TiO_2

Photovoltaic properties of DSSCs

To prove the accuracy of the above assumption for the complexes as co-sensitizers, **1**/N719 and **2**/N719 were fabricated with a stepwise co-sensitization procedure by sequentially immersing the TiO_2 electrode (with thickness of ca. 10 μm) in separate solution of prepared

complexes and N719. For comparison purpose, devices sensitized by individual dye N719 were also fabricated under the same experimental conditions. As shown in Fig. 9, the photocurrent-voltage (*J-V*) characteristic of the DSSCs devices under illumination (AM 1.5 G, 100 mW cm^{-2}) displayed that the conversion efficiency (η) value of individually N719 sensitized device is 6.52% (with J_{sc} = 15.36 mA cm^{-2}, V_{oc} = 0.73 V, and *FF* = 0.58). This low performance compared to the previous reports could be due a single thin transparent TiO_2 film used in these devices. The individually **1** and **2** sensitized devices exhibited η value of 1.87% (with J_{sc} = 4.66 mA cm^{-2}, V_{oc} = 0.65 V, and *FF* = 0.61) and 1.97% (with J_{sc} = 4.89 mA cm^{-2}, V_{oc} = 0.66V, and *FF* = 0.61), respectively. The lower η value for devices sensitized by the complexes sensitizers individually is obviously attributed to their narrow adsorption bands. However, the cell co-sensitized by **1**/N719 and **2**/N719 exhibited the better overall conversion efficiency (η) of 7.82% (with J_{sc} = 18.13 mA cm^{-2}, V_{oc} =0.74 V, and *FF* = 0.58) and 8.39% (with J_{sc} = 18.40 mA cm^{-2}, V_{oc} = 0.75 V, and *FF* = 0.61), which are 19.94% and 28.68% higher than that of cells individually sensitized by N719. The corresponding cells performances are summarized in Table 3. According to the results of test, the higher η value of co-sensitized solar cell compared with the individually N719 sensitized devices is attributed to the enhanced photovoltaic parameters J_{sc} and V_{oc}.

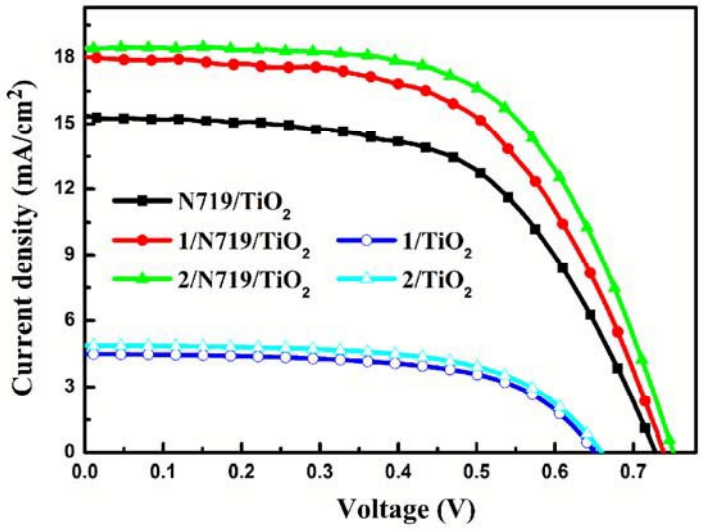

Fig. 9 *J–V* curves for DSSCs based on co–sensitized photoelectrodes and individual N719, **1**, **2** sensitized photoelectrode under irradiation.

Table 3 *J-V* performance of DSSCs based on different photoelectrodes

Photoelectrode	J_{sc}/mA/cm^2	V_{oc}/V	*FF*	η/%
N719/TiO_2	15.36	0.73	0.58	6.52
1/TiO_2	4.66	0.65	0.61	1.87
2/TiO_2	4.89	0.66	0.61	1.97
1/N719/TiO_2	18.13	0.74	0.58	7.82
2/N719/TiO_2	18.40	0.75	0.61	8.39

The results mentioned above are also supported by dark current-voltage (*J-V*) measurements of different devices, which are presented in Fig. 10. It could provide useful information regarding the back electron transfer process by making a comparison of dark current between the investigated cells. It shows that the dark current is lower for the co-sensitized system compared with that of single N719 sensitized DSSC, which is in the order of **2**/N719 < **1**/N719 < N719. The reduction of the dark current demonstrated that **1** and **2** successfully suppress the electron back reaction with I_3^- in the electrolyte by forming a compact layer with N719.

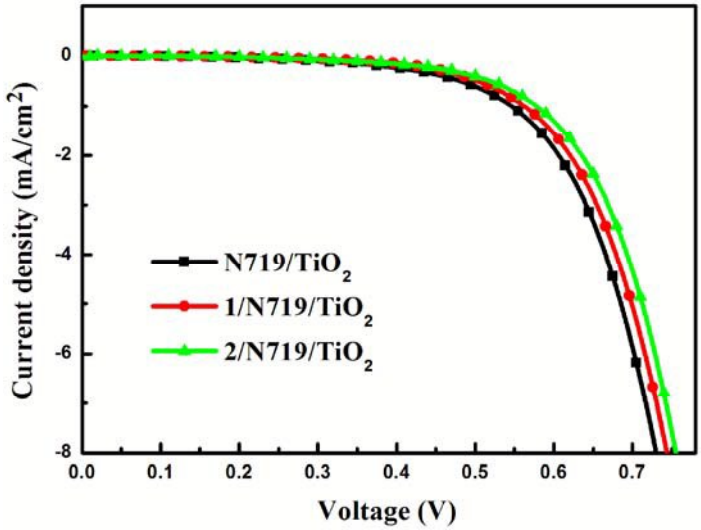

Fig. 10 *J–V* curves for DSSCs based on co–sensitized photoelectrodes and N719 sensitized photoelectrode in dark.

The incident photon–to–current conversion efficiency (IPCE) measurements of different devices were conducted to further understand the effect of co-sensitizers with different complexes on the photocurrent of DSSCs, and the spectra are collected in Fig. 11, which is related by the equation:

$$J_{sc} = \int e\phi_{\text{ph.AM1.5G}}(\lambda)d\lambda$$

where e is the elementary charge and $\phi_{\text{ph.AM1.5G}}$ is the photon flux at AM 1.5 G, 100 mW/cm^2 irradiation.[52–54] The cell individually sensitized by N719 has a 300–750 nm broad IPCE spectrum but in the wavelength range of 340–420 nm the intensity decreases, which is due to the competitive light absorption between I_3^- and N719. When the prepared complex is used as co-sensitizer, this decrease is efficiently inhibited as well as the IPCE spectrum is enhanced in the whole visible region. This is attributed to the fact that co-sensitizers have attached on the TiO_2 surface and contributed to the electron injection into CB of the TiO_2, which is beneficial for light harvesting, electron injection and collection on TiO_2. Based on the IPCE and the absorption spectra, the cell's higher J_{sc} in the case of co-sensitization is mainly ascribed to

better light harvesting in the low wavelength region, where the absorption of N719 is compensated and the competitive light absorption of I_3^- is overcome.

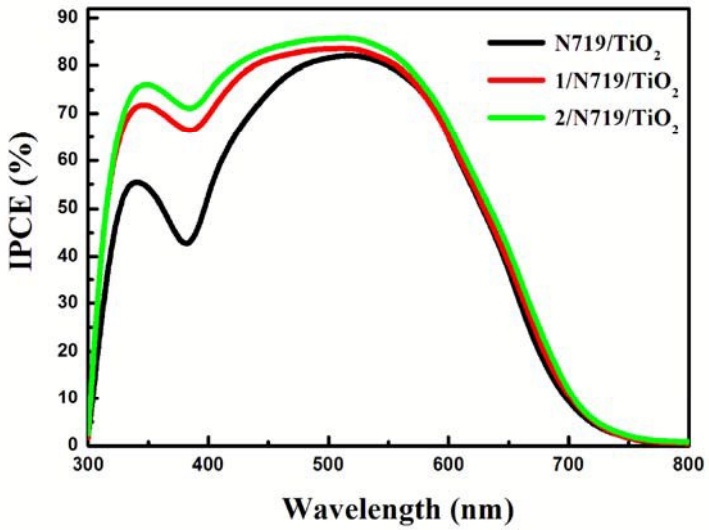

Fig. 11 The incident photon-to-current conversion efficiency spectra of devices based on single N719 sensitized and co-sensitized photoanodes.

Furthermore, to get the information about the electron transport mechanism in different devices, their electrochemical impedance spectra (EIS) were measured under standard AM 1.5 G solar irradiation by applying a forward bias of -0.75V.[55,56] Under light illumination, as shown in Fig. 12a, the two semicircles located in high and middle frequency regions (left to right) are attributed to the electrochemical reaction at the Pt/electrolyte interface and the charge transfer at the TiO_2/dye/electrolyte interface. The radius of the large semicircle located in the middle frequency regions in the Nyquist plots decrease after co-sensitization, and the values are in sequence for **2**/N719 < **1**/N719 < N719, which indicates a decrease in the electron transfer impedance and an increase in the charge transfer rate at this interface after co-sensitization. Above results confirm higher charge transfer rate and lower charge recombination rate are beneficial for enhancing the performance of DSSCs. In dark conditions, as shown in Fig. 12b, the electrons are injected from the FTO substrate into the TiO_2 and the film is charged by electron propagation through the mesoscopic TiO_2 network. Meanwhile, a fraction of the injected conduction band electrons are lost by the reduction of I_3^- ions present in the electrolyte. Therefore, we could measure impedance spectra of DSSCs in the dark to study the electrons recombination from the conduction band of TiO_2 to I_3^- ions. The radius of the large semicircle located in the middle frequency regions in the Nyquist plot increase after co-sensitized with the complexes, and the values are in the order of **2**/N719 > **1**/N719 > N719, which indicates the retardation of the charge recombination between injected electron and I_3^- ions in the electrolyte, with a consequent increase of V_{oc}.

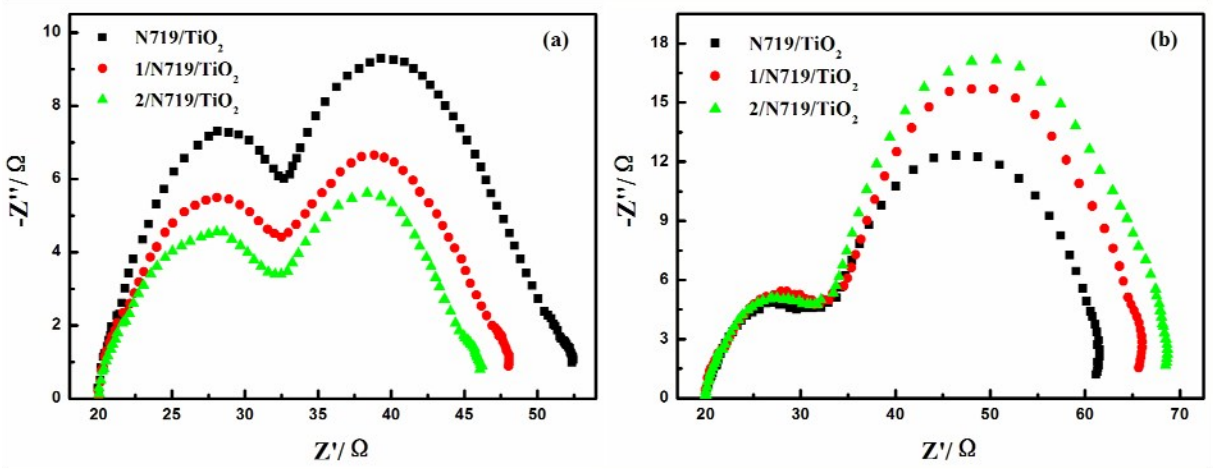

Fig. 12 Nyquist plots of EIS for DSSCs based on different photoelectrodes measured under standard AM 1.5 G solar irradiation (a) or in the dark (b) at forward bias −0.75 V.

In an effort to understand the enhancement of the V_{oc} value in the dye-sensitized solar cells, the electron lifetime (τ_e) in different devices were calculated by fitting the Bode plots of the EIS spectra of different solar cells in dark (Fig. 13), according to the relationship: $\tau_e = 1/(2\pi f_{max})$, where f_{max} is the frequency at the maximum of the curve in the intermediate frequency region in Bode phase plot.[57] The electron lifetime (τ_e) for the devices co-sensitized with **1** and **2** was found to be 18.12 and 20.55 ms, respectively, which are all longer than that of individually N719 sensitized device (13.94 ms). This difference might be expected, since the adsorption of prepared complexes may form a better dye coverage to help to passivate the TiO_2 surface or form an insulating molecular layer composed of prepared complexes and N719 molecules. It will reduce the recombination due to electron back-transfer between TiO_2 and I_3^-. This retardation of the charge recombination between injected electron and I_3^- ions in the electrolyte, leads to a consequent increase of V_{oc}. This appears to be consistent with the larger V_{oc} values sequence which is in the order of **2**/N719 > **1**/N719 > N719.

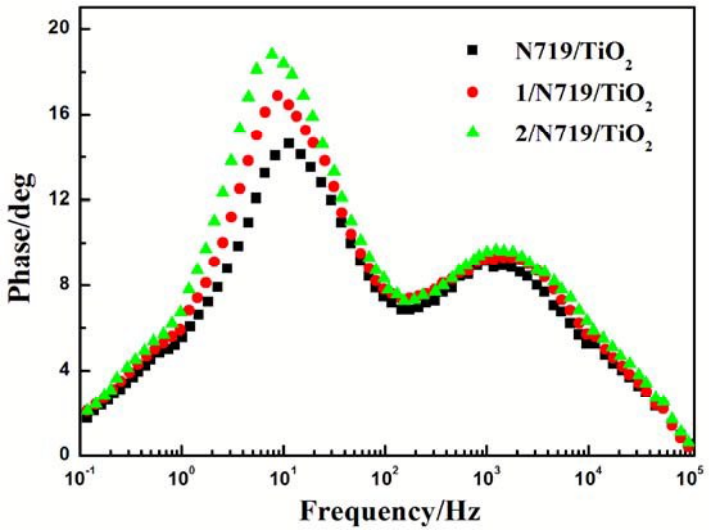

Fig. 13 Bode plots of EIS for DSSCs based on different photoelectrodes measured in dark conditions.

Influence of Structures for DSSCs

Obviously, the strategy of employing the complexes as co-sensitizers to decorate the interface in a TiO_2 photoanode is an efficient method. It has demonstrated that the highly porous nature of the complexes increases the dye loading, and owing to its electrical insulating property the interfacial complex layer suppresses the interfacial charge recombination. The possible photoanode status after co-sensitization is shown in Scheme 2. Furthermore, when the structures of the complexes are taken into account, it is found that there is a relationship between crystal structure and DSSCs performance. First, for complexes **1** and **2**, they adsorbed on Nano TiO_2 thin film surface through carboxyl which has various coordination modes with metal ions, such as bidentate-chelate, bidentate-monatomic, chelate-monatomic, *etc*. Although carboxyl has coordinated to the Cd^{2+} ion in complexes, Ti^{4+} ion may also be coordinated with carboxyl due to the existence of lone pair electrons in carboxylate oxygen atom which could combine with Ti^{4+} ion to form Ti-O coordination bond, and further adsorbed on the TiO_2 film. Second, the nitrogen atoms of organic ligands were expected to adsorb at the Lewis acid sites of the TiO_2 surface. Third, the structure of **1** and **2** contain channel, which can be assembled together to form high surface area arrays for photon collection.[58] Besides the dyes tightly anchored onto the TiO_2 surface ensure the efficiency of photocurrent output, the additional dyes adsorbed onto complexes can contribute to the improvement of conversion efficiency. Compared with 2D lay structure (complex **1**), the presence of 3D framework (complex **2**) may tighten the whole skeleton, thus resulting in much weaker vibrations, which is beneficial to electronic energy transfer. Therefore, the performance of the co-sensitized cell is in the order of **2**/N719 > **1**/N719.[59]

Scheme 2. Possible photoanode status after co-sensitization.

Conclusion

In conclusion, we have reported an interesting a 2D two-fold interpenetrating square lattice layer **1** transformation to a 3D four-fold interpenetrating diamond framework **2** by thermal treatment of the reaction system. Such SCSC transformation process involving the change coordination geometry of central metal and breakage/formation of chemical bonds is quite rare. Meanwhile, the two high dimensional interpenetrating complexes display outstanding photovoltaic performance. **1** or **2** as co-sensitizer has a significant effect on the performance of DSSCs, it could overcome the deficiency of N719 absorption in the region of ultraviolet and blue-violet, offset competitive visible light absorption of I_3^- and reducing charge recombination of injected electron. The co-sensitized device exhibits enhanced performance, and all of them are higher than that of single N719 sensitized solar cells. The special performance for high dimensional interpenetrating complexes as potential light harvesting and energy transferring materials in DSSCs inspires us to further explore the higher photoelectric conversion efficiency in the future.

Acknowledgments

This work was supported by National Natural Science Foundation of China (Grant 21371040, 21571042 and 21171044), the National key Basic Research Program of China (973 Program, No. 2013CB632900). The Fundamental Research Funds for the Central Universities (Grant No. HIT. IBRSEM. A. 201409).

References

1 J. P. Zhang, Y. Y. Lin, W. X. Zhang and X. M. Chen, *J. Am. Chem. Soc.*, 2005, **127**, 14162–14163.

2 C. L. Chen, A. M. Goforth, M. D. Smith, C. Y. Su and H.-C. ȥur Loye, *Angew. Chem. Int. Ed.*, 2005, **44**, 6673–6677.

3 K. Takaoka, M. Kawano, M. Tominaga and M. Fujita, *Angew. Chem. Int. Ed.*, 2005, **44**, 2151–2154.

4 P. Zhu, W. Gu, L. Z. Zhang, X. Liu, J. L. Tian and S. P. Yan, *Eur. J. Inorg. Chem.*, 2008, 2971–2974.

5 J. P. Zhang, P. Q. Liao, H. L. Zhou, R. B. Lin and X. M. Chen, *Chem. Soc. Rev.*, 2014, **43**, 5789–5814.

6 M. Kawano and M. Fujita, *Coord. Chem. Rev.*, 2007, **251**, 2592–2605.

7 G. K. Kole and J. J. Vittal, *Chem. Soc. Rev.*, 2013, **42**, 1755–1775.

8 Z. H. Yan, X. Y. Li, L. W. Liu, S. Q. Yu, X. P. Wang and D. Sun, *Inorg. Chem.*, 2016, **55**,

1096–1101.
9 A. Aslani and A. Morsali, *Chem. Commun.*, 2008, 3402–3404.
10 A. Aslani, A. Morsali and M. Zeller, *Dalton Trans.*, 2008, 5173–5177.
11 Y. M. Song, F. Luo, M. B. Luo, Z. W. Liao, G. M. Sun, X. Z. Tian, Y. Zhu, Z. J. Yuan, S. J. Liu, W. Y. Xu and X. F. Feng, *Chem. Commun.*, 2012, **48**, 1006–1008.
12 S. K. Ghosh, W. Kaneko, D. Kiriya, M. Ohba and S. Kitagawa, *Angew. Chem. Int. Ed.*, 2008, **47**, 8843–8847.
13 X. M. Wang, R. Q. Fan, L. S. Qiang, P. Wang, Y. L. Yang and Y. L. Wang, *Dalton Trans.*, 2014, **43**, 16152–16155.
14 L. H. Cao, Y. S. Wei, H. Xu, S. Q. Zang and T. C. W. Mak, *Adv. Funct. Mater.*, 2015, **25**, 6448–6457.
15 S. K. Ghosh, J. P. Zhang and S. Kitagawa, *Angew. Chem. Int. Ed.*, 2007, **46**, 7965–7968.
16 J. J. Zhang, L. Wojtas, R. W. Larsen, M. Eddaoudi and M. J. Zaworotko, *J. Am. Chem. Soc.*, 2009, **131**, 17040–17041.
17 S. S. Han, L. L. Shi, K. Li, S. Zhao, B. L. Li and B. Wu, *RSC Adv.*, 2015, **5**, 107166–107178.
18 S. Yuan, Y. K. Deng and D. Sun, *Chem. Eur. J.*, 2014, **20**, 10093–10098.
19 D. S. Chen, L. B. Sun, Z. Q. Liang, K. Z. Shao, C. G. Wang, Z. M. Su and H. Z. Xing, *Cryst. Growth Des.*, 2013, **13**, 4092–4099.
20 S. Yuan, Y. K. Deng, W. M. Xuan, X. P. Wang, S. N. Wang, J. M. Dou and D. Sun, *CrystEngComm*, 2014, **16**, 3829–3833.
21 D. Sun, L. L. Han, S. Yuan, Y. K. Deng, M. Z. Xu and D. F. Sun, *Cryst. Growth Des.*, 2013, **13**, 377–385.
22 J. Z. Zhang, W. R. Cao, J. X. Pan and Q. W. Chen, *Inorg. Chem. Commun.*, 2007, **10**, 1360–1364.
23 G. X. Liu, X. F. Wang, H. Zhou and S. Nishihara, *Inorg. Chem. Commun.*, 2011, **14**, 1444–1447.
24 L. Y. Zhang, Y. L. Yang, R. Q. Fan, P. Wang and L. Li, *Dyes Pigm.*, 2012, **92**, 1314–1319.
25 R. Medishetty, L. L. Koh, G. K. Kole and J. J. Vittal, *Angew. Chem. Int. Ed.*, 2011, **50**, 10949–10952.
26 M. H. Xie, X. L. Yang and C. D. Wu, *Chem. Eur. J.*, 2011, **17**, 11424–11427.
27 Y. C. He, J. Yang, G. C. Yang, W. Q. Kan and J. F. Ma, *Chem. Commun.*, 2012, **48**, 7859–7861.
28 L. Wen, P. Cheng and W. B. Lin, *Chem. Commun.*, 2012, **48**, 2846–2848.

29 S. Gao, R. Q. Fan, X. M. Wang, L. S. Qiang, L. G. Wei, P. Wang, Y. L. Yang, Y. L. Wang and T. Z. Luan, *RSC Adv.*, 2015, **5**, 43705–43716.

30 G. M. Sheldrick, S_{HELXL} 97 Program for Crystal Structure Refinement; University of GÖttingen, GÖttingen, Germany, 1997.

31 G. M. Sheldrick, S_{HELXL} 97 Program for Crystal Structure Solution; University of GÖttingen, GÖttingen, Germany, 1997.

32 A. L. Spek, *J. Appl. Crystallogr.*, 2003, **36**, 7–13.

33 A. L. Spek, PLATON, A Multipurpose Crystallographic Tool; Utrecht University: Utrecht, The Netherlands, 2006.

34 Y. Song, R. Q. Fan, X. M. Wang, S. Gao, X. Du, P. Wang and Y. L. Yang, *CrystEngComm*, 2016, **18**, 1878–1882.

35 L. L. Han, T. P. Hu, K. Mei, Z. M. Guo, C. Yin, Y. X. Wang, J. Zheng, X. P. Wang and D. Sun, *Dalton Trans.*, 2015, **44**, 6052–6061.

36 H. Aggarwal, P. Lama and L. J. Barbour, *Chem. Commun.*, 2014, **50**, 14543–14546.

37 D. Sun, M. Z. Xu, S. S. Liu, S. Yuan, H. F. Lu, S. Y. Feng and D. F. Sun, *Dalton Trans.*, 2013, **42**, 12324–12333.

38 S. Gao, R. Q. Fan, L. S. Qiang, P. Wang, S. Chen, X. M. Wang and Y. L. Yang, *CrystEngComm*, 2014, **16**, 1113–1125.

39 S. Chen, Y. K. Wu, Y. Zhao and D. N. Fang, *RSC Adv.*, 2015, **5**, 72009–72018.

40 F. F. Zhao, H. Dong, B. B. Liu, G. J. Zhang, H. Huang, H. L. Hu, Y. Liu and Z. H. Kang, *CrystEngComm,* 2014, **16**, 4422–4430.

41 L. L. Han, X. Y. Zhang, J. S. Chen, Z. H. Li, D. F. Sun, X. P. Wang and D. Sun, *Cryst. Growth Des.*, 2014, **14**, 2230–2239.

42 D. B. Kuang, S. Ito, B. Wenger, C. Klein, J. E. Moser, R. Humphry-Baker, S. M. Zakeeruddin and M. Grätzel, *J. Am. Chem. Soc.*, 2006, **128**, 4146–4154.

43 X. J. Sang, J. S. Li, L. C. Zhang, Z. J. Wang, W. L. Chen, Z. M. Zhu, Z. M. Su and E. B. Wang, *ACS Appl. Mater. Interfaces*, 2014, **6**, 7876–7884.

44 G. D. Sharma, S. P. Singh, R. Kurchania and R. J. Ball, *RSC Adv.*, 2013, **3**, 6036–6043.

45 L. G. Wei, Y. L. Yang, R. Q. Fan, P. Wang, Y. W. Dong, W. Zhou and T. Z. Luan, *J. Power Sources*, 2015, **293**, 203–212.

46 H. L. Jia, X. H. Ju, M. D. Zhang, Z. M. Ju and H. G. Zheng, *Phys. Chem. Chem. Phys.*, 2015, **17**, 16334–16340.

47 L. G. Wei, Y. L. Yang, Z. Y. Zhu, R. Q. Fan, P. Wang, Y. W. Dong and S. Chen, *RSC Adv.*, 2015, **5**, 96934–96944.

48 C. M. Cardona, W. Li, A. E. Kaifer, D. Stockdale and G. C. Bazan, *Adv. Mater.*, 2011, **23**, 2367–2371.

49 G. Boschloo, L. Halggman and A. Hagfeldt, *J. Phys. Chem. B*, 2006, **110**, 13144–13150.

50 S. H. Fan, X. F. Lu, H. Sun, G. Zhou, Y. J. Chang and Z. S. Wang, *Phys. Chem. Chem. Phys.*, 2016, **18**, 932–938.

51 K. R. Justin Thomas, Y. C. Hsu, J. T. Lin, K. M. Lee, K. C. Ho, C. H. Lai, Y. M. Cheng and P. T. Chou, *Chem. Mater*., 2008, **20**, 1830–1840.

52 Y. Z. Wu and W. H. Zhu, *Chem. Soc. Rev.*, 2013, **42**, 2039–2058.

53 Y. Hua, H. D. Wang, X. J. Zhu, A. Islam, L. Y. Han, C. J. Qin, W.-Y. Wong and W.-K. Wong, *Dyes Pigm.*, 2014, **102**, 196–203.

54 L. Q. Ming, H. Yang, W. J. Zhang, X. W. Zeng, D. H. Xiong, Z. Xu, H. Wang, W. Chen, X. B. Xu, M. K. Wang, J. Duan, Y. B. Cheng, J. Zhang, Q. L. Bao, Z. H. Wei and S. H. Yang, *J. Mater. Chem. A*, 2014, **2**, 4566–4573.

55 X. H. Miao, K. Pan, Y. P. Liao, W. Zhou, Q. J. Pan, G. H. Tian and G. F. Wang, *J. Mater. Chem. A*, 2013, **1**, 9853–9861.

56 L. G. Wei, Y. Na, Y. L. Yang, R. Q. Fan, P. Wang and L. Li, *Phys. Chem. Chem. Phys.*, 2015, **17**, 1273–1280.

57 V. M. Guérin, J. Elias, T. T. Nguyen, L. Philippe and T. Pauporté, *Phys. Chem. Chem. Phys.*, 2012, **14**, 12948–12955.

58 S. Gao, R. Q. Fan, X. M. Wang, L. S. Qiang, L. G. Wei, P. Wang, H. J. Zhang, Y. L. Yang and Y. L. Wang, *J. Mater. Chem. A*, 2015, **3**, 6053–6063.

59 D. Y. Lee, I. Lim, C. Y. Shin, S. A. Patil, W. Lee, N. K. Shrestha, J. K. Lee and S.-H. Han, *J. Mater. Chem. A*, 2015, **3**, 22669–22676.